Contents lists available at ScienceDirect

Geochimica et Cosmochimica Acta

journal homepage: www.elsevier.com/locate/gca

The effect of temperature on the release of silicon, iron and manganese into seawater from resuspended sediment particles

Wen-Hsuan Liao [a,b,c,*], Hélène Planquette [a], Brivaëla Moriceau [a], Christophe Lambert [a], Floriane Desprez de Gesincourt [a], Emmanuel Laurenceau-Cornec [a], Géraldine Sarthou [a], Thomas Gorgues [d]

[a] CNRS, Univ Brest, IRD, Ifremer, LEMAR, Plouzané, France
[b] Department of Earth Sciences, National Cheng Kung University, Tainan, Taiwan
[c] Department of Ocean Systems (OCS), Royal Netherlands Institute for Sea Research (NIOZ), Texel, the Netherlands
[d] LOPS, IUEM, IRD, Ifremer, CNRS, Université de Brest, Brest, France

ARTICLE INFO

ABSTRACT

Sediments are considered to be refractory materials with limited influences on dissolved iron (dFe) pool in the ocean. However, recent field observations and laboratory experiments suggest that iron released from resuspended sediment particles and transported from continental margins is prone to fertilize large areas of the world ocean. Here we conducted a dissolution experiment to quantify the amount of dFe released from two types of resuspended sediments (silicate and calcite-rich) to open ocean surface seawater under two temperatures (5 and 15 °C). We followed pH, dissolved oxygen (dO$_2$), phosphate, silicate, dissolved Fe and Mn concentrations (dFe and dMn), and bacterial abundance over 250 days. Extremely low and undetectable phosphate concentrations ($<$50 pmol kg^{-1}) were measured throughout the duration of the experiment, causing limited bacteria growth and stable pH and dissolved O$_2$ concentrations under all conditions. Silicate and dFe concentrations increased through time and high temperature (15 °C) induced more iron dissolution from the two sediments than low temperature (5 °C). Temperature had no effect on the dissolution of Mn. Our results further show that Fe and Mn are not released concurrently from the sediment source and that their distribution can be very different. Scavenging of Fe likely caused a decrease of dFe observed during the experiment, which was probably linked to the formation of Mn oxides. We also observed elevated dissolved Fe isotope ratios after dissolution, around +0.16 to +0.27‰. Isotopically heavy Fe was released from sediments to the dissolved pool during the dissolution but no difference in Fe isotope ratios was observed between the two temperature conditions. The Fe isotope fractionation can likely be attributed to ligand complexation and scavenging of Fe. These two mechanisms can be important factors not only in controlling the amount of Fe released from sediments but also in fractionating Fe isotopes at the sediment–seawater boundary.

1. Introduction

Iron (Fe) is a critical micronutrient in the oceans that is required by phytoplankton for different biogeochemical processes, such as photosynthesis, respiration, and nitrogen fixation (Twining and Baines, 2013). In the open ocean, the dominant supply of Fe to the surface waters has been traditionally considered to be aeolian inputs (Jickells et al., 2005). In coastal areas, Fe supply reaches the oceans mainly from riverine inputs, but these inputs have often been considered to be preserved in sediments (Chester and Jickells, 2012; Poulton and Raiswell, 2002).

Sediments have been considered to be refractory materials with limited contribution to the oceanic dissolved Fe pool. However, some previous studies reported that Fe from continental shelves and sediments can be an important and underestimated Fe source to the ocean (Elrod et al., 2004; Laës et al., 2003; Mackey et al., 2002). In the past decade, several field observations further suggested that sedimentary Fe pool can fertilize large areas of the Pacific, Atlantic and Southern Oceans (Jeandel et al., 2011; Lam et al., 2020; Milne et al., 2017; Nishioka et al., 2020; van der Merwe et al., 2015). It has been proposed that reductive and non-reductive dissolution processes control the amount and variability

---

of dissolved Fe input from marine sediments to the ocean. These two types of sediment dissolution have significantly different Fe isotope signatures (Homoky et al., 2013; Labatut et al., 2014). Reductive dissolution occurs during early diagenetic oxidation of organic carbon and produces a significant amount of reduced, soluble, and isotopically light Fe with Fe isotope composition (δ^{56}Fe) values ranging from -3.31 to -1.73‰ (Homoky et al., 2009; John et al., 2012; Klar et al., 2017; Severmann et al., 2010). Non-reductive dissolution produces unfractionated or slightly heavy isotopic compositions of dissolved Fe with δ^{56}Fe values ranging from -0.01 to $+0.53$‰ in some oxygenated regions of the open ocean (Homoky et al., 2013; Labatut et al., 2014; Radic et al., 2011). We still lack understanding regarding the relative contribution from non-reductive and reductive sedimentary Fe sources to the dissolved Fe pool as well as their cycling processes at the sediment–seawater boundary, so the potential impact from sedimentary Fe inputs cannot be well simulated in global biogeochemical models (König et al., 2021). Indeed, an intercomparison study of global biogeochemical models (Tagliabue et al., 2016) shows a wide range of simulated dissolved Fe distributions, reflecting a lack of agreement regarding Fe cycling processes and input fluxes between considered models. For example, sedimentary Fe input fluxes span a huge range of two order of magnitude difference from 0.6 to 155 Gmol yr^{-1} (Tagliabue et al., 2016). To better quantify the contribution of sedimentary Fe inputs to the ocean at the global scale, a recent parameterization of sedimentary particulate Fe sources and transport (Beghoura et al., 2019) has been added to the global biogeochemical model PISCES-v2 coupled to the Nucleus for European Modelling of the Ocean (NEMO) (Aumont et al., 2015). This model configuration used experimentally-derived sedimentary Fe dissolution rates (Cheize et al., 2019) to gauge the impact of the sedimentary Fe input globally and confirmed the large potential impact of sedimentary Fe sources on dissolved Fe patterns and subsequent control on phytoplankton distribution globally (Beghoura et al., 2019). In particular, the offshore transport combining dissolution of sedimentary particulate Fe could be an efficient process supplying dissolved Fe to the open ocean. While this study proved the importance of resuspended sediments as continuous Fe seeders to the open ocean, the effects of environmental factors, such as light, bacterial abundance, or temperature, on the kinetics of sedimentary Fe dissolution were not investigated. Temperature in particular can shape microbial growth and productivity patterns observed in the ocean (Raven and Geider, 1988) and a recent study showed that Fe solubility in dust increases under high temperature conditions (Félix-Bermúdez et al., 2020).

In this context, we conducted an experiment to quantify the amount of dissolved Fe released from biogenic silicate and calcite rich sediments to open ocean surface seawater under two different temperature conditions (5 and 15 °C). During this 250-day experiment, we followed the evolution of pH, dissolved oxygen, phosphate, silicate, dissolved Mn and Fe concentrations (dMn and dFe), and bacterial abundance to study the mechanisms regulating sedimentary Fe dissolution. Furthermore, we measured both dissolved and particulate Fe isotope composition at the beginning and the end of the experiment to investigate the Fe isotope fractionation caused by the dissolution.

2. Materials and methods

2.1. Experimental setting

The dissolution experiments were conducted in 10-L low density polyethylene (LDPE) and polycarbonate (PC) carboys (Nalgene) over a 250-day period. All the materials used in this study were previously cleaned following GEOTRACES protocols (https://www.geotraces.org/methods-cookbook/) and all manipulations were carried out in a Class 100/ISO 5 clean laboratory to minimize contamination issues. An open ocean surface seawater was collected during the HERMINE cruise at 40 m depth of station 1 in the Atlantic Ocean (44°40′W 23°15′N, https://doi.org/10.17600/17000200). This surface seawater was filtered

through acid-cleaned 0.2 μm filter cartridges (Pall Acropak or Sartorius Sartobran 300), and stored in several 20-L acid cleaned polypropylene carboys (Nalgene) for three years before our experiment. Surface seawater possesses the advantage of a low dissolved Fe concentration (0.17 nM), which allowed us to observe an obvious change of trace metal concentrations in a fairly short time scale. Besides, in the real ocean, sediment particles can be possibly transported to the surface waters. Two sediments from the Kerguelen plateau, named A3 and C11, were used in this study, both of them were collected during the KEOPS-1 cruise (Blain et al., 2008), freeze-dried then stored in 50 mL polypropylene centrifuge tubes (Falcon) until use in this experiment (Blain et al., 2007). Sediment A3 is a biogenic silicate rich sediment and C11 is a calcite rich sediment with distinct Si, Fe and Mn concentrations (Table 1). It should be noted that their full elemental compositions are provided in Cheize et al. (2019), together with the sampling details. In brief, the experimental design consisted in adding ~50 mg of sediment into 11 L of seawater to mimic the concentration of suspended particles (~5 mg L^{-1}) in benthic nepheloid layer (Gross et al., 1988; Puig et al., 2013). Choosing the same sediments with the same concentrations as Cheize et al., 2019 allowed us to directly compare our results, and to observe any noticeable changes within one year of experiment. Nonetheless, this particle concentration is at the high end of particle concentrations reported in very active benthic nepheloid layers (Gardner et al., 2018). Yet, those particles concentrations are not unrealistic, as pointed out in Puig et al. (2013). They showed that an event can trigger sediment resuspension and increase particle concentrations to ~6 mg/L, a value comparable to our experimental condition. Moreover, the Kerguelen Plateau is likely to interact strongly with the Antarctic Circumpolar Current, leading to intense steered jets (e.g. Dove et al., 2021), resulting in high resuspended particle concentrations.

After the sediment addition, the carboys were sealed during the entire period. To follow the hydrographical changes and dissolved trace metal concentrations, an acid-cleaned PTFE tube (1/8 in.) mounted with PTFE threaded fittings and plug (Upchurch) were designed to subsample the seawater, and the details of the setting can be found in Fig. 1 of Cheize et al. (2019). Several orbital shakers (Edmund Bühler GmbH) were used to mix the overlying seawater without disturbance of sediments under a stir rate set at 50 rpm during the experiment, this rate being close to previous studies which used 32 rpm (Hammond et al., 2004) or 60 rpm (Pratihary et al., 2014). As the sea surface temperature ranges from 0 to 15 °C in most of the high nutrient low chlorophyll regions, we decided to keep all the carboys in a temperature-controlled room (15 °C) and a dedicated temperature-controlled incubator (5 °C), both under dark condition to minimize the influence from the production of organisms.

Table 1
Experimental conditions designed for this study and initial particulate and dissolved Si, Fe, and Mn concentrations. Treatment I and II were used to check the differences potentially caused by carboy materials and dissolved oxygen sensor spot. Treatments II and III were designed to monitor the effect of temperature.

Initial concentrations			
	dSi (μmol L^{-1})	dFe (nmol L^{-1})	dMn (nmol L^{-1})
Seawater	0.65	0.17	1.43
	pSi (μmol L^{-1})	pFe (nmol L^{-1})	pMn (nmol L^{-1})
A3	56	920	14
C11	31	810	25
Treatment[#]	I.*	II.*	III.
Temperature (°C)	15	15	5
Carboy material	LDPE	PC	PC
Sediment type	A3	A3 and C11	A3 and C11
dO$_2$ monitoring	No	Yes	Yes

[#] All the carboys were maintained in the dark during the 250-day experiment.
* Controls were carried out both in LDPE and PC carboys at 15 °C under dark condition with 2.5 L of seawater. We assume that at 5 °C seawater is more stable than 15 °C, so controls were only carried out at 15 °C.

An optical oxygen sensor (PreSens, SP-PSt3-NAU-D5-YOP) was used in all the PC carboys to monitor dissolved oxygen concentrations. The sensors were intercalibrated with the sensor used in the French SOMLIT program, NKE-MP7, maintained at LEMAR/IUEM, and the NKE sensor has been calibrated by Winkler method (https://www.somlit.fr/). Before conducting the experiment, a trace metal leaking test was conducted to evaluate possible trace metal leak from the sensor spots. The sensor spots were placed in 125 mL natural seawater for 3 months (in triplicate). The dMn and dFe concentrations were 1.13 ± 0.05 and 0.08 ± 0.04 nmol kg^{-1} without the sensor spot, and 1.19 ± 0.04 and 0.12 ± 0.01 nmol kg^{-1} with the sensor spots, respectively. These small dissolved Mn and Fe contributions of 0.06 ± 0.06 and 0.04 ± 0.04 nmol kg^{-1}, respectively, from the sensor spot only account for 1.2 and 2.9% of final dMn and dFe concentrations and are deemed negligible. All the concentration values mentioned above are average values (n = 3) ± one standard deviation.

In addition to dissolved oxygen concentrations (dO$_2$), we followed the changes of several variables through the entire period, including pH, silicate, phosphate, dissolved Fe, dissolved Mn, and bacterial abundance. Before conducting the experiment, we measured the Fe isotope composition in the surface seawater (5 L) and in the two sediments (bulk digested). During the first 100 days, we sampled weekly, then biweekly for the remaining of the experiment (Table 1). Sampling resulted in no more than 15% loss of seawater volume in each carboy by the end of the 250-day experiment. At the end of the experiment, sediments were recovered on a filter (Supor 47 mm, 0.45 μm) by filtration of the remaining seawater (around 9.8 L) to measure their Fe isotope composition.

2.2. Seawater monitoring

pH- The variation of pH during the incubation was followed with a Mettler-Toledo pH meter (±0.01 pH units; temperature compensated) and glass electrode, regularly calibrated against 4.01, 6.87 and 9.18 buffer solutions (25 °C; Bioblock Scientific).

Silicate and phosphate – The samples were immediately filtered through Millex mixed esters membrane filters (0.22 μm) and stored at 4 °C (silicate, 5 mL) and −20 °C (phosphate, 10 mL) before analysis. Then silicate and phosphate concentrations were measured with an auto-analyzer AA3 HR SEAL-BRAN + LUEBBE following the colorimetric methods of Aminot and Kérouel (2007). The detection limits were 0.030 and 0.014 μmol kg^{-1} for silicate and phosphate, respectively. The method was certified using the Reference Material for Nutrients in Seawater (Kanso Lots CD and CJ).

Heterotrophic bacteria abundance – Duplicate 2 mL samples were fixed with glutaraldehyde (0.25% final concentration) and then stored at −80 °C immediately after sampling. Analyses were performed using a flow cytometer (FCM) FacsVerse (Becton-Dickinson®, San Jose, USA), set on medium flowrate (around 80 μL min^{-1}) for 30 sec. FCM analysis were run all along the 250-day experiment (from three times a month to once according to sampling schedule intensity). Briefly, samples were gently thawed, then diluted 10 times in filtered sterile seawater (450 μL + 50 μL sample) and incubated 10 min in the dark after addition of 5 μL of a 1/100 dilution in Milli-Q water of the SYBR® Green I commercial solution (DNA permeant probe, Molecular Probes, #S7563). Heterotrophic bacteria were detected on flow-cytometer cytograms according to their size and complexity (side scatter and forward scatter values of the flow cytometer) and their green fluorescence (SYBR® Green probe). Heterotrophic bacteria were easily distinguished from autotrophic cells, which present a red fluorescence due to the presence of chlorophyll. Heterotrophic bacteria abundance was presented by an average value from the duplicate measurement (n = 2 ± confidence interval 95%).

Dissolved Mn and Fe – Fifteen mL of seawater was immediately filtered through Millex mixed esters membrane filters (0.22 μm) and acidified with ultrapure HCl (Merck) at each sampling time. The dissolved Mn and Fe concentrations were measured inline using a seaFAST

pico preconcentration system (ESI) coupled with sector field inductively coupled plasma mass spectrometry (SF-ICP-MS, Element XR). The details about reagent preparation and concentration determination can be found in Tonnard et al. (2020). We used acidified Milli-Q water as blanks, with values of 0.010 ± 0.002 and 0.083 ± 0.024 nmol kg^{-1}, for dMn and dFe, respectively (average ± 1 standard deviation, n = 30). The detection limits for dMn and dFe were 0.005 and 0.073 nmol kg^{-1}, respectively (three times of the standard deviation). Both blanks and detection limits are comparable to the values reported in previous studies (Lagerström et al., 2013; Tonnard et al., 2020). Accuracy was determined from the analysis of consensus (GSP and GSC) and certified (NASS-6) seawaters (Table 2). Reproducibility was assessed through the standard deviation of replicate measurements of consensus seawater samples, which were 10% and 8% for dMn and dFe, respectively (Table 2). The Mn concentrations of reference materials obtained in this study are slightly lower than the consensus values, which might be related to the differences between sampling bottles for GSP and GSC or due to the slightly low pH during preconcentration. The recovery of Mn is relatively sensitive to pH between 5 and 6 (Sohrin et al., 2008), so a pH value slightly lower than 6 may cause slightly low recovery of Mn during preconcentration.

2.3. Determination of Fe isotope composition in seawater and sediments

We carried out replicate measurements to obtain dissolved and particulate Fe isotope composition at the beginning and at the end of the experiment in the bulk sediments and in seawater. Fe isotope analysis was carried out by double spike technique. Detailed technical procedures for seawater samples are described in Conway et al. (2013) and detailed procedures for trace metal preconcentration and Fe purification from sediment samples can be found in Table S1 of Liao et al. (2021). In brief, Fe concentrations were first determined to calculate the amount of double spike solution needed. Then, a double spike solution of ^{57}Fe-^{58}Fe was added to samples with a sample to spike ratio of 1 to 2 with the double spike composition of 0.002% ^{54}Fe, 0.66% ^{56}Fe, 49.5% ^{57}Fe, 49.8% ^{58}Fe. For seawater samples (around 2 L), trace metals were concentrated on a Nobias PA1 resin and the anion exchange procedure was conducted by using AG-MP 1 M following the procedure used in Liao et al. (2020). For sediment samples, we conducted a two-step total digestion on 10 mg of each sediment by using a mixture of concentrated ultrapure HNO$_3$ and HF, then a mixture of concentrated ultrapure HCl and HNO$_3$ to obtain bulk Fe concentrations, then carried out twice the anion-exchange procedure to purify Fe to get bulk Fe isotope compositions (Liao et al., 2021). At the end of the experiment, sedimentary particles were collected using Sterifil aseptic filtration system (Millipore) and 47 mm acid-cleaned 0.2 μm polyethersulfone filter, then sediment particles were easily removed from the filter by acid-cleaned tweezers to obtain ~10 mg for bulk digestion. The overall recovery for Fe was over 90% for both seawater and sediment samples. The Fe blanks for processing 2 L acidified Milli-Q were 0.40 ± 0.15 and 0.70 ± 0.03 ng (average ± 1 standard deviation) for trace metal preconcentration and anion exchange procedure, respectively. The overall blank is two orders of magnitude lower than the sample mass used (minimum 100 ng Fe) to determine the Fe isotope composition. The δ^{56}Fe measurements were conducted using a Neptune multi-collector inductively coupled plasma mass spectrometer (Thermo Fisher Scientific) with a PFA integrated nebulizer (150 μL min^{-1}; Elemental Scientific) and Apex-Q (Elemental Scientific) introduction system at the Pôle Spectrométrie Océan, Ifremer. X-type Ni sampler and H-type skimmer cones were used to conduct the analyses. δ^{56}Fe was measured under high resolution with a typical ^{56}Fe sensitivity, 4 V per 100 ppb. The signal voltages were measured on the left flat shoulder of the combined metal-argide peak, based on the technique of Weyer and Schwieters (2003). Solutions of pure standard (IRMM-014), pure spike, and mixtures of three different sample-to-spike ratios (2 to 1, 1 to 2, and 1 to 4) were analyzed for data reduction at the beginning of each analytical batch. Stable isotopic

Table 2

Dissolved Mn and Fe concentrations of the consensus and certified (*) reference seawaters used in this study (average ± 1 standard deviation).

CRM		GSP			GSC			NASS-6*		
		Average	SD	n	Average	SD	n	Average	SD	n
[Mn]	This study	0.62	0.06	16	1.69	0.21	6	8.28	0.58	12
(nmol kg^{-1})	*Consensus*	*0.78*	*0.03*	–	*2.18*	*0.08*	–	*9.65*	*0.91*	–
[Fe]	This study	0.16	0.01	16	1.26	0.10	6	8.65	0.58	12
(nmol kg^{-1})	*Consensus*	*0.16*	*0.05*	–	*1.54*	*0.12*	–	*8.86*	*0.82*	–

ratios were calculated from an average of 30 cycles using a data reduction scheme based on Siebert et al. (2001). The isotopic ratios of each sample were obtained from the averaged value of duplicate analyses. A standard-sample bracketing method was also used to monitor the instrument condition during the analysis, so mixtures of standard (IRMM-014) and spike were designed to match [Fe] and sample-to-spike ratio of samples and were used to bracket every five samples. δ^{56}Fe are expressed in per mil (‰) relative to IRMM-014 using delta notation as described in the following Eq. (1):

$$d^{56}Fe = \left[\left(^{56}Fe/^{54}Fe \right)_{sample} / \left(^{56}Fe/ ^{56}Fe \right)_{IRMM-014} - 1 \right] \times 10^3 \quad (1)$$

The internal error of each sample (2σ) was calculated by the propagated error for each individual analysis with two bracketing standards (Conway et al., 2013). The theoretical source of errors in isotopic composition analysis by double spike technique includes errors from counting statistics, Johnson noise, and isobaric interference (John, 2012). Our measured errors matched well with the theoretical error calculated from Monte Carlo simulation (John, 2012), showing reliable external accuracy (Fig. 1). This method was first verified by determining the isotope composition of the international standard NIST 3126a, which yielded a δ^{56}Fe value of +0.35 ± 0.14‰ (2 standard deviations, n = 60 with different working concentrations, Fig. 1), consistent with the reported value of +0.39 ± 0.13‰ (Rouxel and Auro, 2010). Then we determined the δ^{56}Fe value in several certified reference materials (CRM) with different matrices (Table 3), which were comparable to the previous studies. Most of the samples were analyzed under working concentrations higher than 200 ppb (Fig. 1) to obtain relatively small errors.

3. Results

Throughout the 250-day sediment dissolution experiment, the composition of seawater evolved differently as a function of time

Table 3

The Fe isotope composition of the certified reference materials measured in this study (Average ± 2 standard deviation).

CRM	Matrix	This study	Ref. value
SLRS-4 (n = 2)	River water	0.40 ± 0.09	0.48 ± 0.11[a]
SLEW-3 (n = 2)	Estuarine water	−0.18 ± 0.18	−0.10 ± 0.21[a]
BCR-2 (n = 5)	Basalt	0.11 ± 0.10	0.11 ± 0.03[b]
PACS-3 (n = 3)	Marine sediment	0.20 ± 0.07	–
BCR-414 (n = 3)	Plankton	−0.02 ± 0.07	–

[a] Rouxel and Auro (2010).
[b] Craddock and Dauphas (2011).

depending on the sediments added and the temperature conditions. In this section, we first describe the variation of dissolved O_2 (dO_2, μmol L^{-1}), pH and bacteria abundance (cell mL^{-1}), then the temporal variation of silicate (μmol kg^{-1}), dFe, and dMn (nmol kg^{-1}) through time. As described in Table 1, Treatment I was designed to check the potential difference caused by different carboy materials. As all the parameters observed in the LDPE and PC carboys were comparable (Fig. S1), our discussion is focused on the results obtained using PC carboys (Treatments II and III presented in Table 1). Due to a limited amount of low dFe seawater and also limited space on orbital shakers, we could not carry out duplicates for each treatment. However, from the comparable patterns of all the parameters observed in LDPE and PC carboys under exactly the same conditions (Figs. 2, 3, and S1), suggesting an acceptable reproducibility.

3.1. Temporal variation of dissolved oxygen concentration, bacterial abundance, and pH

The saturated dO_2 at 15 and 5 °C were 313 and 399 μmol L^{-1}, respectively and remained fairly stable during 250 days (Fig. 2). The average dO_2 of the controls, A3 (15 °C), C11(15 °C), A3 (5 °C), and C11
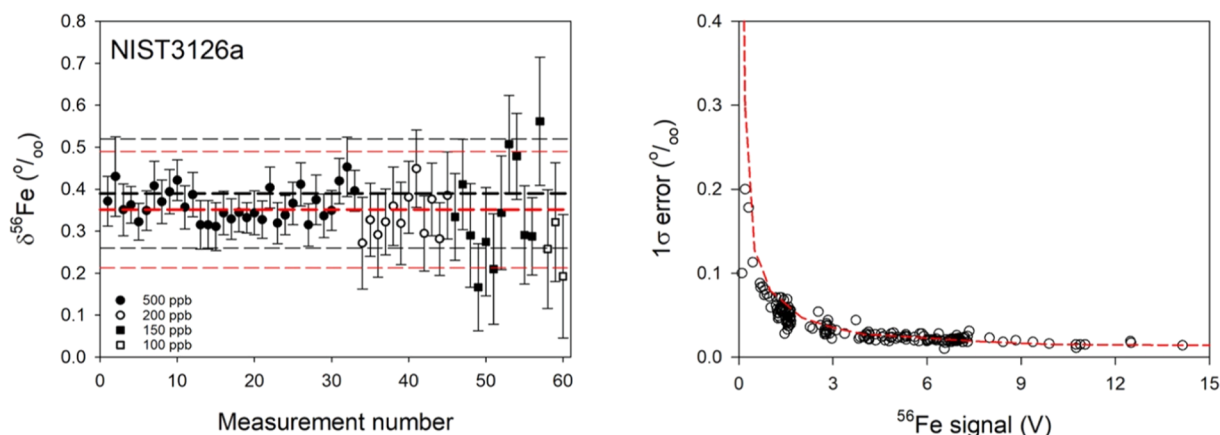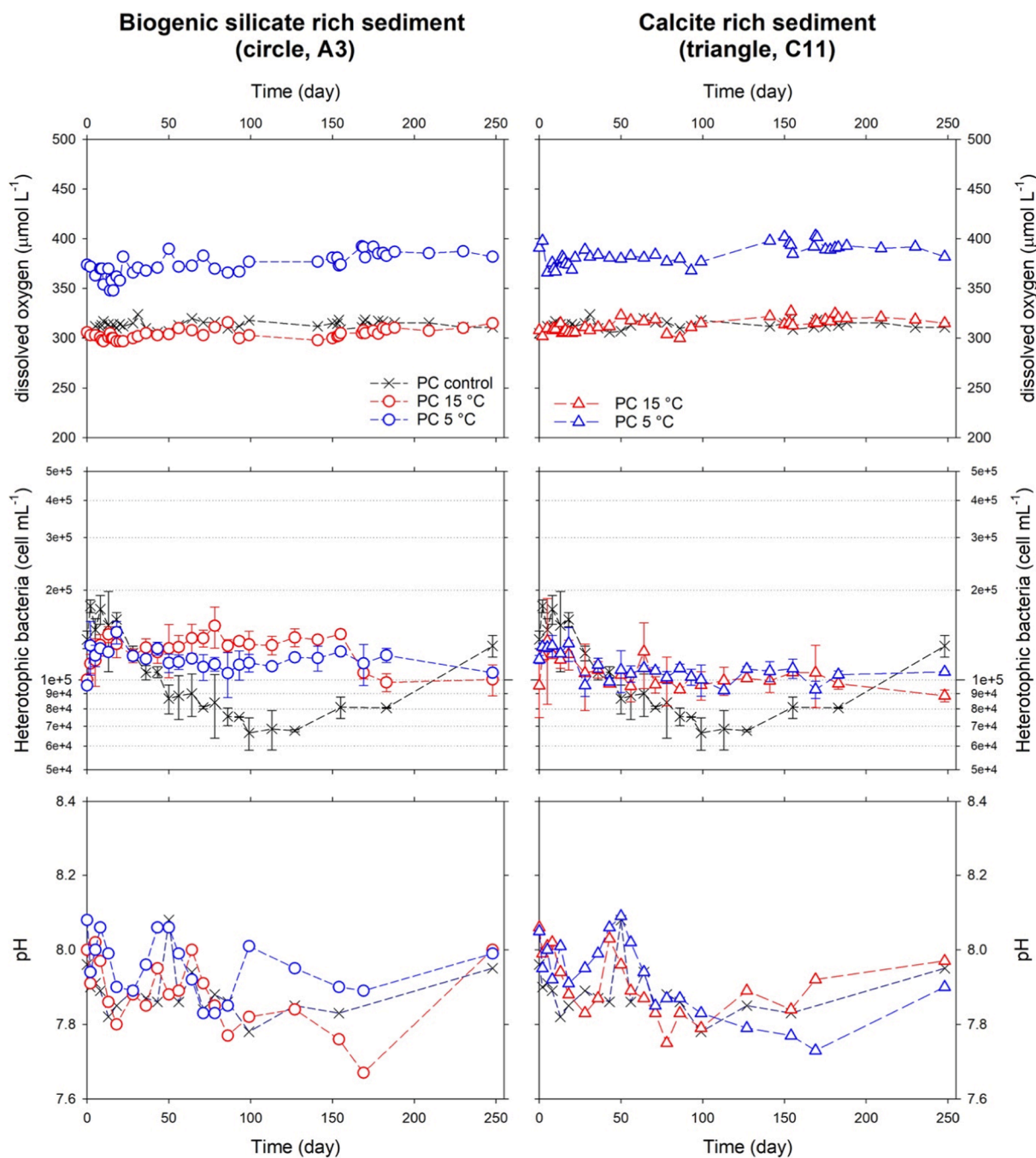

Fig. 1. The reproducibility of NIST-3126a measurements (left panel) and theoretical 1σ internal error (dashed red line) versus measured internal error (black circles) with ^{56}Fe intensity (right panel). (Left) Thick and thin dashed lines are the average δ^{56}Fe value with 2 standard deviations. The red lines are the values obtained in this study (0.35 ± 0.14‰ calculated from all the data points in the figure); the black one (0.39 ± 0.13‰) is from Rouxel and Auro (2010). The concentration in ppb stands for the working concentration summarized from both sample and spike. (Right) Theoretical values were calculated using Monte Carlo simulation (John, 2012), assuming sample to spike ratio of 1 to 2. The black circles stand for 1σ internal standard error obtained from all the measurements performed in this study.

Fig. 2. The temporal variation of dissolved oxygen concentration (dO$_2$, µmol L^{-1}), bacterial abundance (cell mL^{-1}), and pH values during the 250-day sediment dissolution experiment. The left and right panels show the results obtained by using biogenic silicate and calcite rich sediments, respectively (circles and triangles). Red and blue symbols represent data collected under 15 and 5 °C treatments, and black crosses for the control treatment.

(5 °C) were 313 ± 4, 304 ± 5, 313 ± 6, 374 ± 11, and 384 ± 10 µmol L^{-1}, respectively, showing no significant variations of dO$_2$ during the experiment. This result is probably due to the absence of biological activity, also suggested by the constant bacterial abundance of around 10^5 cells mL^{-1} in all conditions (Fig. 2), which is one order of magnitude lower than the values reported in Cheize et al. (2019). This discrepancy may be attributed to the different initial concentrations of nutrients in seawaters used in these two studies. We used an oligotrophic Atlantic surface seawater, with phosphate concentrations between 0.04 and 0.08 µmol kg^{-1} in the first 56 days then decreasing under the detection limit (0.014 µmol kg^{-1}), and with initial silicate concentration of 0.70 ± 0.03 µmol kg^{-1} (Supplementary file). Cheize et al. (2019) used a nutrient

replete surface seawater collected in the Southern Ocean with an initial silicate concentration of 11.7 µmol kg^{-1}, but they did not measure phosphate or nitrate concentrations. The initial high silicate concentration implies that high nutrient concentration (nitrate and phosphate) could have supported the growth of bacteria observed in their study. In terms of pH values, the values of all conditions decreased during the first 18 days then went back to the initial values at around day 50. After day 50, the values decreased again and varied between 7.7 and 8.0. The pH values in all conditions kept around the same value by the end of the experiment.

3.2. Temporal variation of silicate (dSi), dissolved Mn (dMn), and dissolved Fe (dFe)

The initial silicate concentration (dSi) was 0.70 ± 0.03 µmol kg^{-1} in all conditions, and remained stable in the control treatment during the 250-day experiment. Temperature (15 and 5 °C) had a significant impact on sedimentary silicate dissolution for the two types of sediments (Fig. 3). For the biogenic silicate rich sediment (A3), dSi at 15 °C increased through time and ultimately reached 9.5 µmol kg^{-1} while dSi at 5 °C increased up to only 3.0 µmol kg^{-1} at the end of the experiment (Fig. 3). For the calcite rich sediment, similar trends were observed, with

dSi values reaching 4.4 and 1.0 µmol kg^{-1} under 15 and 5 °C conditions, respectively (Fig. 3). The silicate dissolution rates of the two sediments (A3 and C11) were roughly 4-fold and 10-fold higher at 15 °C than at 5 °C (Table 4). At 15 °C, about 16% of particulate silica was released from the biogenic silicate rich sediment to the seawater, while only 0.65% of particulate silica was released from the calcite rich sediment at 5 °C. These results show that the silicate dissolution is dependent on the initial sediment composition and on the temperature.

We also followed the evolution of dissolved Fe and Mn concentrations. For biogenic silicate rich sediment (A3), the dissolved Fe concentration increased through time particularly during the first 78 days,
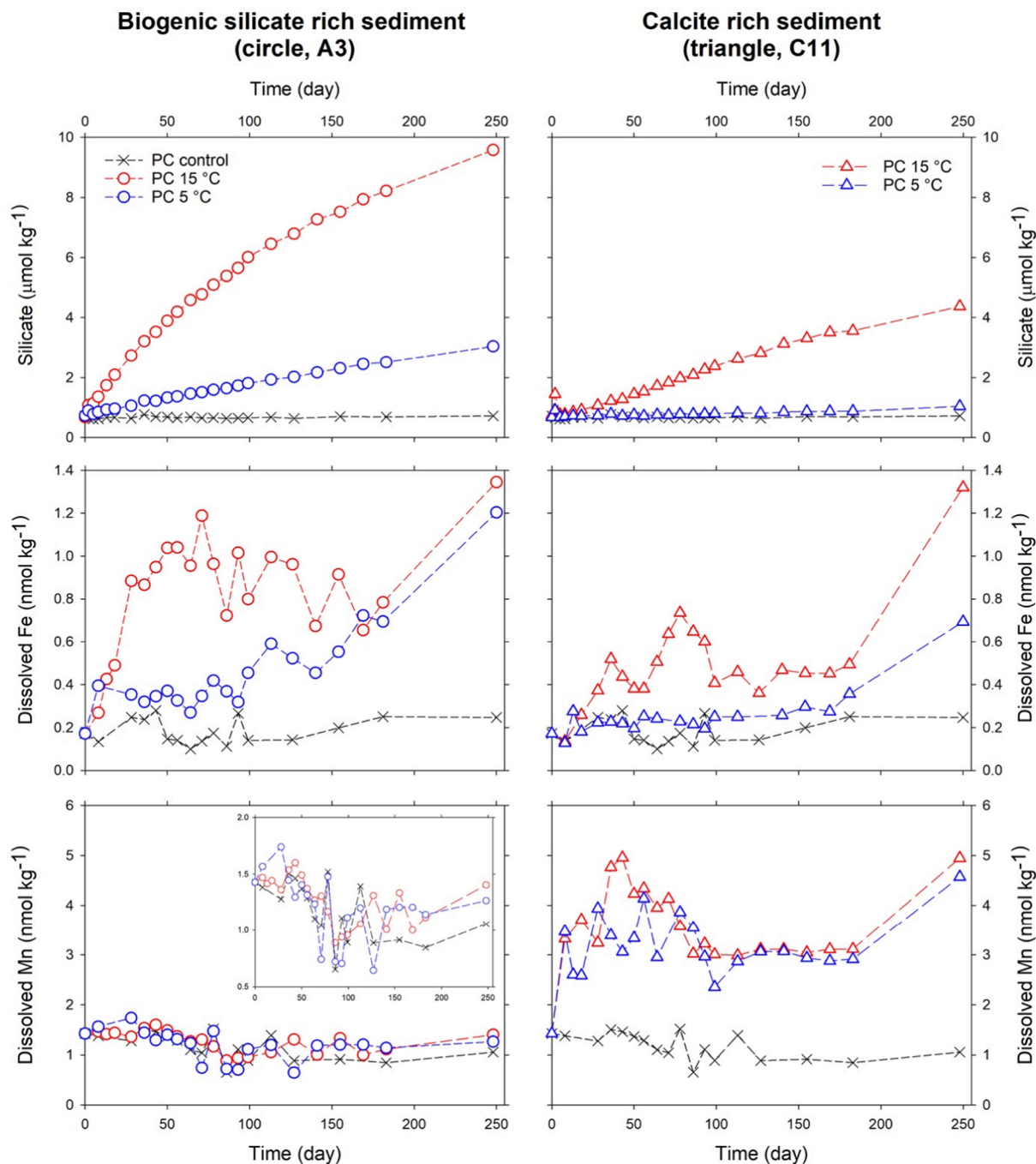

Fig. 3. The temporal variation of silicate (µmol kg^{-1}), dissolved Fe (nmol kg^{-1}), and dissolved Mn (nmol kg^{-1}) during the 250-day sediment dissolution experiment. The colour and symbol codes are based on the ones used in Fig. 2. The left and right panels show the results obtained by using biogenic silicate and calcite rich sediments, respectively (circles and triangles). Red and blue symbols represent data collected under 15 and 5 °C treatments, and black crosses for the control treatment.

Table 4
A summary of mean dissolution/scavenging rates, the variation of dissolved concentrations of silicate, Fe, and Mn, and the percentage increased/decreased of the initial particulate stock of each element at the end of the experiment.

			15 °C		5 °C	
	Element	Unit	A3	C11	A3	C11
Mean dissolution rate (scavenging, −)	dSi	nmol kg^{-1} d^{-1}	35.09	14.52	9.25	1.44
	dFe	pmol kg^{-1} d^{-1}	4.53	4.59	4.12	2.09
	dMn	pmol kg^{-1} d^{-1}	−0.10	14.08	−0.65	12.58
Dissolved concentration increased (decreased, −)	ΔdSi	μmol kg^{-1}	8.77	3.63	2.31	0.36
	ΔdFe	nmol kg^{-1}	1.13	1.15	1.03	0.52
	ΔdMn	nmol kg^{-1}	−0.02	3.52	−0.16	3.14
Particulate stock dissolved (scavenged, +)	pSi	%	15.73	6.51	4.15	0.65
	pFe	%	0.12	0.14	0.11	0.06
	pMn	%	+0.18	14.36	+1.18	12.83

reaching around 1.3 nmol kg^{-1} at 15 °C (Fig. 3). After day 78, dFe abruptly decreased to around 0.6 nmol kg^{-1}, then increased again at the end of the experiment. For the calcite rich sediment (C11), dFe had a similar evolution pattern but with lower concentrations (0.7 nmol kg^{-1} on day 78 at 15 °C). We found that higher temperature induced more Fe dissolution through time (Fig. 3 and Table 4). On the contrary, the effect of temperature was insignificant on sedimentary Mn dissolution for both sediment types (Fig. 3). Under the two temperature settings, dMn were basically comparable with the control values for the biogenic silicate rich sediment (A3), and the value slightly decreased at the end of the experiment (Fig. 3). More dMn was released from the calcite rich sediment C11 (Fig. 3 and Table 4), but the evolution pattern and concentration levels were identical under the two temperature settings (Fig. 3). In the Section 3.1, we mentioned that pH values dropped in the beginning of the experiment. No correlation exists between pH and the two dissolved trace metals (Fig. S2), indicating that the change of pH was not related to Fe or Mn dissolution from sediments to seawater.

3.3. The initial and final dissolved and particulate Fe isotope compositions

As shown in Fig. 4, the initial δ^{56}Fe values were +0.31 ± 0.11 (n = 3) and +0.26 ± 0.10 (n = 3)‰ in the biogenic silicate and calcite rich sediments; the initial value for seawater was +1.21 ± 0.12‰. At the end
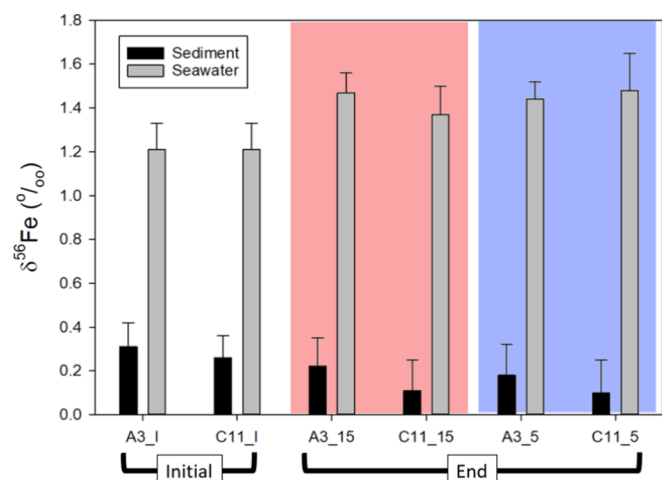

Fig. 4. Fe isotope composition in seawater and sediments at the beginning and the end of the experiment. The red and blue areas highlighted the high and low temperature conditions, respectively (15 and 5 °C).

of the experiment, the particulate δ^{56}Fe values were +0.22 ± 0.13 (15 °C) and +0.18 ± 0.14‰ (5 °C) for the biogenic silicate rich sediment (A3); the values were +0.11 ± 0.14 (15 °C) and +0.10 ± 0.15 (5 °C) for the calcite rich sediment (C11). The dissolved values at the end of the experiment were +1.47 ± 0.09 (15 °C) and +1.44 ± 0.08‰ (5 °C) for A3, and +1.37 ± 0.13 (15 °C) and +1.48 ± 0.17‰ (5 °C) for C11. All the Fe isotope compositions mentioned above were the average of replicate measurements with 2 standard deviations. Overall, the Fe isotope compositions of sediments A3 and C11 are comparable before and after dissolution experiment, as values overlap within 2 standard deviations. At the end of our experiment, the dissolved Fe isotope composition increased by +0.16 to +0.27‰ depending on the conditions. The bulk δ^{56}Fe values in sediments determined in this study (Fig. 4) are similar to the values of bulk sediments ranging from −0.03 to +0.16‰ from the cape margin (Homoky et al., 2013) and the average value of +0.14 ± 0.07‰ from the Western Equatorial Pacific reported in Labatut et al. (2014). In surface waters, as the fractionation mechanisms and the sources are extremely diverse, the surface dissolved δ^{56}Fe values span a large range from −0.74 to +0.78‰ (Labatut et al., 2014). The highest surface value (0 ~ 200 m) reported in the North Atlantic Ocean was +0.80 ± 0.07‰ (Conway and John, 2014); the one in the Southern Ocean reached to +1.28 ± 0.39‰ (Ellwood et al., 2020), confirming that the initial dissolved δ^{56}Fe value we determined was consistent with literature data (Fig. 4).

4. Discussion

4.1. Processes controlling Si, Fe, and Mn dissolution

To further investigate the kinetics of the release of Si, Fe, and Mn from sediments, we calculated the dissolution rate constant (d^{-1}) using two models, including a commonly used one-step dissolution process and a two-different-phase dissolution approach. These two models were used to study silicate dissolution (Boutorh et al., 2016; Greenwood et al., 2001; Moriceau et al., 2009) in the past and we also applied in this study for calculating Si, Fe, and Mn dissolution rates (Fig. 5).

The first model is a simple first-order rate equation and assumes a one-step dissolution process (equation (2)), where X can be Si, Fe, or Mn. pX_t is the left-over particulate elemental concentration (μmol kg^{-1}) at a given time t (day), pX_0 is the initial total particulate elemental concentration (μmol kg^{-1}) calculated by the sediment mass used for this experiment (~50 mg) and elemental concentrations given in Table 1 of Cheize et al. (2019), and k is the dissolution rate constant (d^{-1})

$$pX_t = pX_0 e^{-kt} \tag{2}$$

We can then obtain the amount of dissolved elemental concentration released from particles to calculate the left-over particulate elemental concentration (equation (3)), where dX_t is the dissolved elemental concentration at a given time t and dX_0 is the initial dissolved elemental concentration (μmol kg^{-1}).

$$pX_0 - (dX_t - dX_0) = pX_0 e^{-kt} \tag{3}$$

After a simple logarithm conversion (equation (4)), we can obtain the dissolution rates (k) of all treatments through a linear regression of our data:

$$ln\left[\frac{pX_0 - (dX_t - dX_0)}{pX_0}\right] = -kt \tag{4}$$

The second model we applied to our data is a two-phase dissolution model (Eqs. (5a) and (5b)), which can represent two different phases of a certain element dissolving one after the other (e.g., one protecting the other), or changes in dissolution rates through time or induced by modification of environmental conditions (e.g., temperature). The parameters are basically the same as used in previous equations: in Eqs. (5a) and (5b), at substitution time t_s (day), the dissolution constant
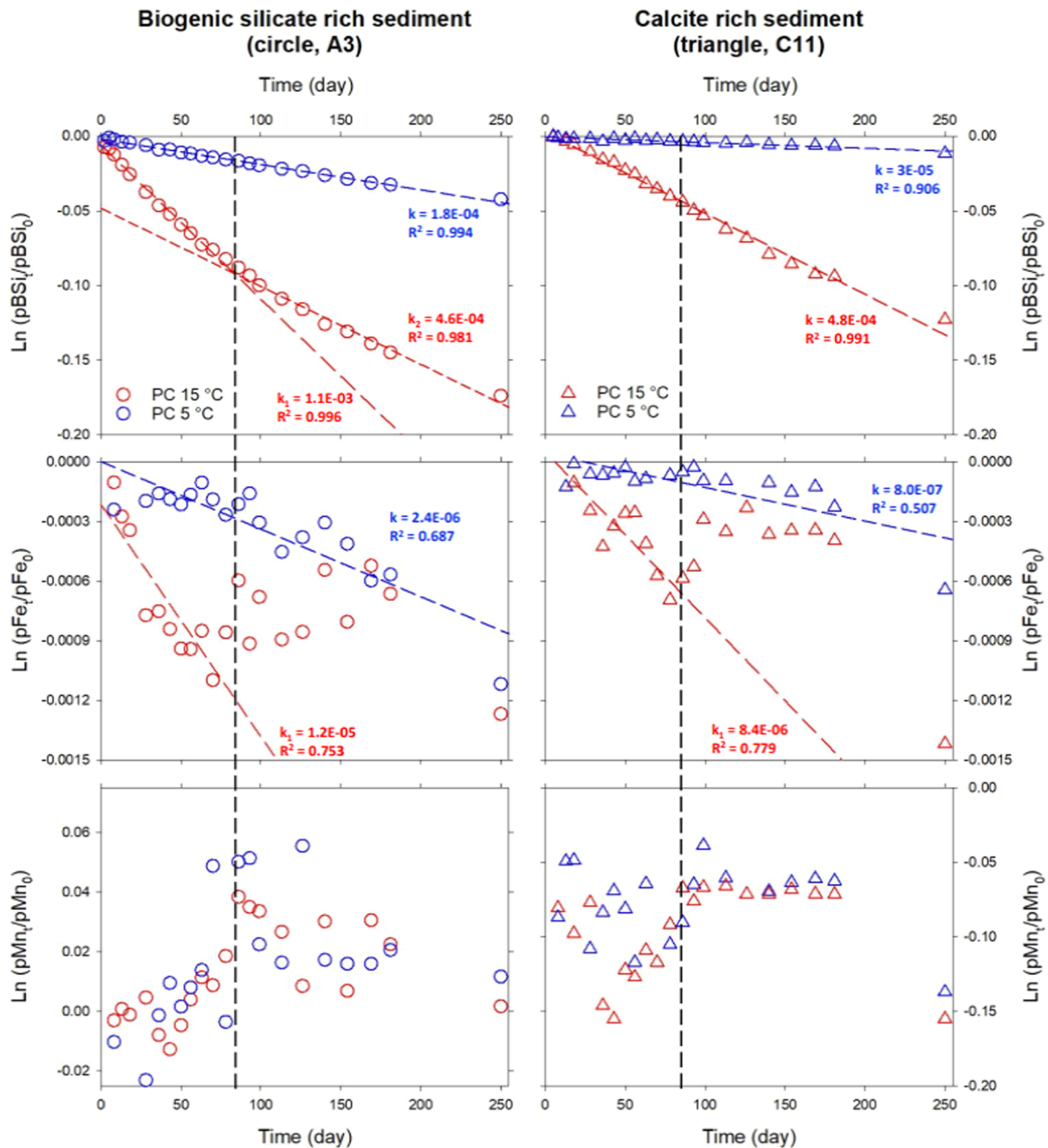
Fig. 5. Derived concentration changes of particulate Si, Fe, and Mn at each sampling step relative to the initial values during the 250-day sediment dissolution experiment (two dissolution models were used to demonstrate the dissolution patterns, see text for details). The colour and symbol codes are based on the ones used in Figs. 2 and 3. Based on the elemental dissolution patterns, we divided the experimental time into two different stages by using the black dashed lines: stage one – a fast Si and Fe dissolution stage with Mn oxide formation and stage two – a slow Si dissolution and Fe scavenging stage with no or some Mn oxide formation. The red and blue dashed lines shown in the panels represent the linear regression of data points of different stages, and their slopes represent the dissolution or scavenging rates at the certain stage.

changes from k_1 to k_2 (d^{-1}), with the particulate elemental concentration at time t_s (X_{ts}, µmol kg^{-1}).

$$pX_t = pX_0 e^{-k_1 t}; 0 < t < t_s \qquad (5a)$$

$$pX_t = pX_{t_s} e^{-k_2(t-t_s)}; t > t_s \qquad (5b)$$

4.1.1. Si, Fe, and Mn dissolution patterns and rates

   Using the derived particulate concentration change of the three elements, Fig. 5 shows the patterns of Si, Fe and Mn dissolution with their dissolution rates (k) that can be determined from the slopes of linear

regression lines (log-based ratios versus time plots, Eq. (4)). For the biogenic silicate rich sediment (A3), at 15 °C, the best fit dissolution model is the two-phases model: we obtained good regression (R^2 = 0.996 and 0.981) by using the two-phases model. A fast dissolution of 1.1×10^{-3} d^{-1} occurred in the first 78 days and associated with dissolved Fe release of 1.2×10^{-5} d^{-1}. This was followed by a relatively slow Si dissolution of 4.6×10^{-4} d^{-1} and no dFe release until the end of the experiment, due to a possible Fe reincorporation/adsorption back to the biogenic silica phase (Fig. 5). Previous culture studies found that Fe can be incorporated into diatom frustules (de Jonge et al., 2010; Ellwood

and Hunter, 2000), confirmed by one field study in the Southern Ocean (Ingall et al., 2013). When calculating dissolved Fe to Si ratios through time (Fig. 6), for A3, we observed that most of the dissolved Fe to Si ratios varied between 0.2 and 0.3 mmol mol^{-1} during the first 78 days (Fig. 5), which are slightly lower than but close to the average ratios of 0.33 mmol mol^{-1} obtained from measuring Fe incorporation inside biogenic silica in Ingall et al. (2013). The ratios then decreased to around 0.1 mmol mol^{-1} after day 78, which means that Fe dissolution did not follow silicate dissolution at this stage. Furthermore, the decrease of Fe concentrations points to adsorption processes.

At 5 °C treatment, the one stage model worked best, with a Si dissolution constant of 1.8×10^{-4} d^{-1} (R^2 = 0.991) and we also observed relatively stable Fe to Si ratios (Fig. 6). These results probably imply that the Fe and Si dissolution originate from a slow dissolution phase, probably related to the second stage of dissolution at 15 °C. Indeed, their Si dissolution rates were at the same order of magnitude with the values of 1.8×10^{-4} and 4.6×10^{-4} d^{-1} for 5 °C and the slow one at 15 °C, respectively. At both temperature conditions, Mn was adsorbed during the first 78 days with an average rate of 5.5×10^{-4} d^{-1} for both temperatures then concentrations remained stable until the end of the experiment.

For the calcite rich sediment (C11), the basic one-step model was the best fit for the silicate dissolution, under both temperatures (Fig. 5, R^2 = 0.991 and 0.906 at 15 and 5 °C, respectively). At 15 °C, a two-stage pattern was also observed for Fe and Mn, but this pattern was not related to Si dissolution. At 5 °C, only one steady dissolution of Fe with a rate of 8.0×10^{-7} d^{-1} was observed. Dissolved Mn concentrations fluctuated during the first 78 days then reached stable values, like for A3. At 5 °C, the variations of Fe to Si ratios remained relatively small during dissolution (Fig. 6). However, Mn dissolution was higher for calcite rich sediment (Fig. 3), implying that Mn may play a much more important role in regulating Fe dissolution or scavenging, which is discussed in Section 4.2.2. Our results suggested that the calcite rich sediment (C11) tends to release more dissolved Mn into seawater, while the biogenic silicate rich sediment (A3) tends to adsorb dissolved Mn on particles, consistent with the results reported in Cheize et al. (2019).

With both sediments, high temperature induced more silicate dissolution and also increased the dissolution rate constants for roughly one order of magnitude higher than the low temperature (Fig. 5). Yet, the silicate dissolution rate constants derived from this study, ranging from 3.0×10^{-5} to 1.0×10^{-3} d^{-1}, were roughly two to three orders of magnitude lower than the ones derived from the experiment of dead diatom frustule, ranging from 0.07 to 0.23 d^{-1} for the first stage and 0.02 to 0.07 d^{-1} for the second stage (Boutorh et al., 2016). The silicate dissolution from fresh biogenic materials, with fast dissolution rates, is much more important than the ones from sediments.

4.1.2. Scavenging of Fe and Mn oxide formation

Manganese oxides, known as important scavengers, remove several other trace metals from seawater (Goldberg, 1954; Jeandel, 2016). The formation of manganese oxides may be another and probably even more important mechanism to cause both Mn and Fe adsorption in our experiment. For the biogenic silicate rich sediment (A3), the increase of the $\ln(pMn_t/pMn_0)$ values strongly implies that manganese oxide formation occurred during the first 78 days (Fig. 5) with no significant difference of dissolved Mn concentrations under two temperature conditions (Fig. 3). Biological Mn(II) oxidation is faster than abiotic Mn(II) oxidation processes, which suggests that biological Mn(II) oxidation dominates in many environments such as the sediment/seawater interface in the Pacific (Landing and Bruland, 1987), the Black Sea (Lewis and Landing, 1991) and the Gulf of Mexico (Van Cappellen et al., 1998). However, as no significant changes of bacterial abundance was observed in this study (Fig. 2), the biological Mn(II) oxidation cannot be the mechanism explaining the Mn oxide formation found in this study. The fact that the initial dissolved Mn concentration was high, 1.4 nmol kg^{-1}, could have provided a large pool of dissolved Mn and induce Mn oxide formation. These abiotically-formed Mn oxides then could have led to the scavenging of Fe and Mn for the biogenic silicate rich sediment (A3). For the calcite rich sediment (C11), dissolved Mn concentrations increased to around 5 and 4 nmol kg^{-1} under 15 and 5 °C, respectively, during the first 50 days, then decreased to around 3 nmol kg^{-1} from day 100 to 180 (Fig. 3). Based on this Mn dissolution pattern, the formation of Mn oxides may be the mechanism decreasing the Fe dissolution rate and probably stimulating the scavenging of Fe around day 78. To summarize, the dissolution or scavenging of Fe observed in the experiment may be regulated by the interactions between biogenic silica and manganese oxides with Fe. During the first stage (Fig. 5), Fe dissolution plays a much more important role than scavenging of Fe, resulting in a net dissolution effect. During the second stage (Fig. 5), scavenging of Fe can be the dominant process. It should be noted that both dissolution and scavenging occur simultaneously and several factors, such as temperature and interactions between different elements, can determine their relative contribution at different stages of the experiment. In addition, scavenging of Mn on Mn oxides likely occurred during this experiment, but we think Mn oxide formation probably was still the major process to transfer dissolved Mn from dissolved to particulate pool in our experiment.

At the end of our experiment, elevated Fe concentrations in all the treatments and slightly increased Mn concentrations from the calcite-rich sediment treatment were observed. The elevated Fe and Mn concentrations implied that more metals can be released from the sediments. This release could originate from a different particle phase that is much easier to dissolve after the previous two stages observed in this study. However, in order to confirm this hypothesis, a much longer
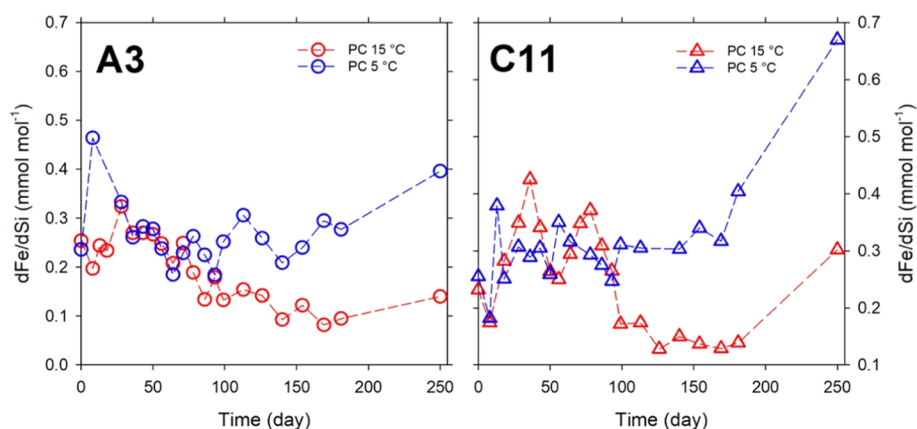

Fig. 6. Temporal evolution of dissolved Fe to Si ratios through time for both sediments and at 15 and 5 °C. The colour and symbol codes are based on the ones used in Fig. 2.

experiment time would be required with XRD and SEM analyses of particles collected at different stages. This would hold great promises to decipher the Fe solubility from different mineral compositions.

Overall, we found that the effect of temperature is significant on the dissolution of Fe from resuspended sediments (Figs. 3 and 5), even though other factors such as scavenging of Fe onto Mn oxides or biogenic silica may also control the Fe dissolution rates. Among those processes, temperature is still the first-order factor to increase Fe dissolution from resuspended sediments. As the temperature conditions range significantly from less than 0 °C at high latitudes to more than 30 °C in tropical regions, the dissolution of Fe from resuspended sediments can be higher in low latitude regions than in the high ones. The effect of temperature was also observed for aerosol Fe dissolution where higher temperatures can induce more and faster Fe dissolution (Félix-Bermúdez et al., 2020). Finally, the initial dFe and dMn concentrations are likely to influence the dissolution rates, and designing experiments with different seawaters with a range of dFe and dMn concentrations would be interesting to perform.

4.2. Decoupled Fe and Mn dissolution kinetics

Our experiment revealed decoupled dissolution kinetics for Fe and Mn. Interestingly, Fe and Mn dissolutions are affected by several factors, including temperature, sediment composition, and internal cycling processes (Figs. 3 and 5). In addition, several studies demonstrated that oxidation kinetics also plays an important role on regulating Fe and Mn interactions in the ocean (Colombo et al., 2021; Hatta et al., 2013; Jensen et al., 2020). Generally, Fe and Mn are considered to be released from the same sources, such as continental margin sediments (Tessin et al., 2020) and hydrothermal vents (González-Santana et al., 2020). Yet, the extent and pace of Fe and Mn release can vary: for example, an experimental study showed that Mn concentrations released from dust were proportional to the added dust amounts, but dissolved Fe reached to a maximum value, independent of the amounts and types of dust added (Mendez et al., 2010). The main underlying hypothesis was that the difference in mineral composition was the factor influencing Mn dissolution while the ligand complexing capacity was the one influencing the most the Fe dissolution (Mendez et al., 2010). Therefore, dissolution kinetics can be different for Fe and Mn, especially at the boundary layer as the environmental conditions and sediment types vary significantly (Burdige, 1993). Furthermore, the formation of Mn (oxyhydr)oxides can be another critical factor to regulate the amount of Fe released from sedimentary or hydrothermal sources. A recent study investigated particulate manganese in the near- and far-field hydrothermal plumes and found that freshly formed Mn oxides in the near-field plume have higher scavenging capacity than the aged Mn oxides in the far-field plume (Lee et al., 2021). These authors further argued that the phenomena in the hydrothermal plumes may be applied elsewhere in the water column. For instance, the freshly formed Mn oxides either from biotic or abiotic processes may have high scavenging capacities, which is particularly important in the surface water. The freshly formed Mn oxides during the first 78 days of this experiment could have quickly scavenged Fe (Figs. 3 and 5). It thus appears that the initial composition of sediments alone has a major effect on Mn dissolution while Fe dissolution is driven by a combination of temperature, sediment types and Mn oxide formation. It is thus critical to study how Mn interacts with the other metals in marine water column and possibly model its biogeochemical cycle with regards to the iron cycle.

4.3. Fe isotope fractionation during the dissolution

In this study, the initial and final $\delta^{56}Fe_{sed}$ of sediment A3 or C11 (Section 3.3) are overlapped within two standard deviations, showing no significant difference (Fig. 4) throughout the course of the experiment. However, for initial and final $\delta^{56}Fe_{sw}$, the differences ($\Delta^{56}Fe_{sw}$ $_{(final - initial)}$) range from +0.16 to +0.27‰ for A3 and C11, respectively.

Interestingly, the difference between dissolved and particulate $\delta^{56}Fe$ signatures, determined in the seawater of the Western Equatorial Pacific – a region strongly influenced by sediment-origin particles (Labatut et al., 2014), has shown the dissolved phase being heavier of +0.27 ± 0.25‰ than the particles. Labatut et al. (2014) argued that the isotopically heavy Fe signature is the result of a net non reductive release of dissolved Fe from the particles, which may also be at play in our experiment. Indeed, we observed an increase of dissolved $\delta^{56}Fe$, which is likely produced by the non reductive iron dissolution of sediment particles. However, it should be stressed that the $\delta^{56}Fe$ difference (between the beginning and the end of our experiment) we observed can not quantitatively be compared to the $\delta^{56}Fe$ difference between the particulate and dissolved phases observed in the field. Yet, such a non-reductive source was also reported by Artigue (2020) in deep waters flowing above the Kerguelen Plateau, resulting in a 4 nM dFe increase compared to background deep waters. Using the data obtained in the thesis mentioned above, we can simply carry out an isotopic mass balance calculation (1.0 nM * −0.2‰ + 4.0 nM$_{(addition)}$ * $\delta^{56}Fe_{addition}$‰ = 5.0 nM * +0.3‰), leading to a $\delta^{56}Fe_{addition}$ of +0.43‰. For our experiment, the mass balance calculation (0.17 nM * 1.2‰ + 1.13 nM $_{(addition)}$ * $\delta^{56}Fe_{addition}$‰ = 1.30 nM * 1.4‰) leads to an $\delta^{56}Fe_{addition}$ of +1.43‰, which also points to net Fe dissolution that has an isotopically heavy signature. This signature is about 1.0‰ heavier than the one observed in the field.

This difference can result from different mechanisms during the experiment, such as scavenging and organic complexation (Abadie et al., 2017). It is well known that >99% of dissolved Fe is rapidly complexed by organic ligands upon transport to the ocean (Gledhill and Buck, 2012, and references therein). Evidence for stabilisation of dissolved Fe in marine systems by organic ligands has been observed in previous studies (Bundy et al., 2014; Homoky et al., 2012; Hopwood et al., 2015) and some studies reported that the $\delta^{56}Fe$ value of organically complexed Fe is around 0.6‰ higher than inorganic Fe (Dideriksen et al., 2008; Morgan et al., 2010), but this difference is likely to be ligand specific and variable. In addition, Fitzsimmons et al. (2017) found that an ligand bound Fe end member in hydrothermally influenced waters is higher in dFe concentration and heavier in isotopic composition than the non-hydrothermal background seawater (+0.66‰ versus −0.10 to −0.22‰), suggesting an hydrothermal-origin ligand binding results with an isotopically heavy fractionation. Thus, the increased final $\delta^{56}Fe$ values may possibly be attributed to the enhancement of heavy Fe binding with organic ligands although we do not have any ligand measurements to support this statement unlike Cheize et al. (2019) study. In addition, Homoky et al. (2021) recently showed that colloidal Fe with $\delta^{56}Fe$ signature of +0.07 ± 0.07‰ is a dominant Fe supply to the ocean and argued that lithogenic weathering is much more important than ligand complexation to produce these colloidal Fe in sediment porewater. However, the Fe concentrations in sediment porewater ranged from 0.01 to 100 μmol kg^{-1} which are significantly higher than the Fe concentrations in seawater (around 1 nmol kg^{-1} in deep waters). Thus, it remains unclear how ligand complexation controls sedimentary Fe dissolution and isotopic fractionation at the ocean-sediment boundary/benthic nepheloid layer and under a wide range of Fe concentrations, from sub-nanomolar to micromolar levels.

In addition to ligand complexation, the scavenging of Fe that likely occurred during the experiment (Figs. 3 and 5) might also fractionate Fe isotopes. However, the effects of scavenging on fractionating Fe isotopes still remain unclear. One study found that scavenging resulted in the fractionation factor of −0.67‰, and this factor was similar to the $\delta^{56}Fe$ difference ($\Delta^{56}Fe_{particle - sw}$) of −0.54‰ observed in their field observation (Ellwood et al., 2015). Another study indicated that the fractionation caused by scavenging can be insignificant with the $\Delta^{56}Fe$ of −0.30 ± 0.31‰ (Radic et al., 2011). Based on the current knowledge, the fractionation of scavenging could be insignificant or cause dissolved $\delta^{56}Fe$ values to be higher than the particulate ones, and the later one is consistent with what we observed in this study.

The final isotopic composition of seawater at the end of our experiment likely reflects the Fe fractionation caused by both ligand complexation and scavenging (Abadie et al., 2017), yet their relative contribution cannot be quantified at this stage. In addition, using sequential leaching, two studies showed that reactive Fe phases present in sedimentary particles may have fundamentally different iron isotope compositions between them and compared to bulk sediment (Henkel et al., 2018; Henkel et al., 2016). It is thus possible that the Fe-hosting phases (e.g. silicates) fractionate differently but we unfortunately do not have data to investigate this. The overall exchange process that preferentially fractionates the heavy Fe-isotopes into solution and, of course, preferentially fractionates the light isotopes into or onto the residual particles needs to be deciphered. The isotope exchange described above would have to occur in parallel to the non-reductive Fe dissolution, which is just one of the mechanisms possibly causing the isotopically heavy fractionation observed in this study. Evaluating the contribution of different Fe phases to the total Fe dissolution and their relationship with Fe isotopic fractionation deserves to be studied in future studies.

In terms of isotopic mass balance at the beginning and the end of the experiment, the particulate Fe pool accounts for over 99.9% of the total Fe amount for all treatments (Table 4), while the dissolved pool only accounts for a small portion (around 0.1% in Table 4). Although we observed the changes of dissolved δ^{56}Fe after the experiment, considering the error propagation from both concentration and isotope composition, the Fe isotope mass calculation is balanced before and after the dissolution and between dissolved and particulate phases, because 99.8% of Fe remain in the particulate pool. This mass balance calculation also implies that, even when only a small portion of Fe is released from the sediment, it could possibly enhance dissolved Fe concentrations and change its isotopic composition.

4.4. Implication for sedimentary Fe fluxes and marine Fe isotope budget

Several studies have pointed out the contribution of non-reductive sedimentary Fe inputs to the water column in the North Atlantic Ocean (Colombo et al., 2021; Conway and John, 2014; Conway et al., 2018). Conway and John (2014) confirmed the importance of non-reductive sedimentary Fe inputs, which may account for a significant portion of total Fe input in the Northwestern Atlantic Ocean. A recent model study compiled literature data, including benthic dissolved iron fluxes, bottom water oxygen, and sedimentary carbon oxidation rates to estimate the global dissolved Fe flux from marine sediments, yielding a flux of 150 ± 75 Gmol Fe yr^{-1} (Dale et al., 2015). The global sedimentary Fe flux is thus significantly higher than the other inputs, such as dust deposition ranging from 1.4 to 32.7 Gmol yr^{-1} (Tagliabue et al., 2016), riverine input around 26 Gmol yr^{-1} (de Baar and de Jong, 2001), and hydrothermal input around 5.2 ± 0.6 Gmol yr^{-1} (Roshan et al., 2020). As we can roughly estimate the global sedimentary Fe flux, we still cannot quantify the relative contributions of non-reductive and reductive sedimentary Fe to the total fluxes. Even though we know the δ^{56}Fe signature of different inputs to the ocean (Labatut et al., 2014), the deep water δ^{56}Fe is not homogeneous in the global ocean (Horner et al., 2020). We thus are still in a very early stage to calculate a marine Fe isotope budget. Most importantly, Fe isotope studies play a critical role to bring the non-reductive dissolution process to light and suggest that it could be a major source at a global scale (Conway and John, 2014; Homoky et al., 2013; Labatut et al., 2014; Radic et al., 2011). This will need to be investigated in further studies.

Regarding the temperature, a study in the Gulf Stream further estimated that the stream driven Fe flux likely from a non-reductive sedimentary Fe input may be on the order of 15% in average (sometimes up to 75%) of dust Fe deposition flux in the region (Conway et al., 2018). Conway et al. (2018) calculated an Fe anomaly of 0.34 nmol kg^{-1} in the upper 300 m water column, where temperature is above 15 °C in the region. Our experiment showed that Fe dissolution under 15 °C can

reach up to 1.1 nmol kg^{-1} for the biogenic silicate rich sediment during the first 78 days. The temperature in the North Atlantic subtropical gyre can further reach a higher level to 25 °C. There, high surface temperatures are likely to induce more Fe dissolution from resuspended particles at low latitudes. In contrast, at high latitudes, Fe dissolution might be inhibited compared to warmer environments. However, other factors, such as sediment type and oxidation kinetics, also control the release of dissolved Fe while modifying the interactions between Fe and Mn. This is especially true in the high latitude regions with low temperatures (Colombo et al., 2021; Hatta et al., 2013; Jensen et al., 2020). At mid-latitudes (~40°N to S) — where conditions of both iron limitation and relatively warm surface temperatures can occur, dissolution of particles have the potential to drive large increase of dFe pool. In the future, the continental slope and shelf regions may be ideal platforms to carry out field/mesocosm studies to pursue the interpretation of findings found in laboratory experiments.

5. Conclusion

We conducted a sediment dissolution experiment to study the effect of temperature on elemental dissolution of Si, Fe, and Mn, from sediments to seawater. Our results demonstrated that high temperature induces more Fe dissolution from resuspended sediments, but not for Mn, and that the elemental dissolution is dependent on different sediment types. Biogenic silicate rich sediments yielded a higher Fe dissolution rate than the calcite-rich sediment while it was the opposite for Mn. Using dissolution models to calculate the elemental dissolution rates, we found a two-stage Si dissolution pattern for the biogenic silicate rich sediment, starting with a fast dissolution then a slow dissolution after 78 days. The elemental dissolution pattern suggests that Fe may be mainly released from the biogenic silica at the first stage. Then we observed the decrease of Fe and Mn and hypothesized that the scavenging of Fe back to particles, likely freshly-formed Mn oxides, may be the cause of the decrease observed at the second stage. In terms of the relationship between Fe and Mn, our results clearly show that Fe and Mn are not released at the same pace from the sediments and that their distribution and cycling processes can be very different. In addition, we found that isotopically heavy Fe was released from the sediments to seawater, causing the δ^{56}Fe differences, around +0.16 to +0.27‰, between the initial and final seawater compositions, which possess a similar isotopically heavy increase trend of non-reductive dissolution. This δ^{56}Fe difference may also be attributed to scavenging processes. This process, as well as ligand complexation, play important roles not only in controlling the amount of Fe released from sediments but also in fractionating Fe isotopes at the sediment–seawater boundary and will require dedicated studies. The isotope exchange causing by different processes would have to occur in parallel to the non reductive Fe dissolution.

Declaration of Competing Interest

The authors declare that they have no known competing financial interests or personal relationships that could have appeared to influence the work reported in this paper.

their invaluable comments, which have profoundly improved the quality of this manuscript. This work was supported by the French National Research Agency in the framework of the BIIM project (ANR-18-CE01-0006).

Appendix A. Supplementary material

Supplementary materials of this manuscript include two supplementary figures (Figure S1 and S2) and all the raw data of the dissolution experiment used to produce figures in this study. In Figure S1, we compared the data obtained by using LDPE and PC carboys and found no significant differences between these two carboys conditions. In Figure S2, we demonstrated that there is no correlation between pH and dissolved trace metals (Fe and Mn) in this study. We also provided all the raw data of the sediment dissolution experiment, including dO$_2$, bacteria abundance, pH, phosphate, silicate, dissolved iron, and dissolved manganese concentrations in the supplementary section. Supplementary material to this article can be found online at https://doi.org/10.1016/j.gca.2023.04.014.

References

Abadie, C., Lacan, F., Radic, A., Pradoux, C., Poitrasson, F., 2017. Iron isotopes reveal distinct dissolved iron sources and pathways in the intermediate versus deep Southern Ocean. Proc. Natl. Acad. Sci. U.S.A 114, 858–863.

Aminot, A., Kérouel, R., 2007. Dosage automatique des nutriments dans les eaux marines : méthodes en flux continu, p. 188.

Artigue, L., 2020. Cycles biogéochimiques océaniques : apports des traceurs élémentaires et isotopiques, l'aluminium et le fer couplés à une approche hydrodynamique.

Beghoura, H., Gorgues, T., Aumont, O., Planquette, H.F., Tagliabue, A., Auger, P.A., 2019. Impact of inorganic particles of sedimentary origin on global dissolved iron and phytoplankton distribution. J. Geophys. Res.Oceans 124, 8626–8646.

Blain, S., Queguiner, B., Armand, L., Belviso, S., Bombled, B., Bopp, L., Bowie, A., Brunet, C., Brussaard, C., Carlotti, F., Christaki, U., Corbiere, A., Durand, I., Ebersbach, F., Fuda, J.L., Garcia, N., Gerringa, L., Griffiths, B., Guigue, C., Guillerm, C., Jacquet, S., Jeandel, C., Laan, P., Lefevre, D., Lo Monaco, C., Malits, A., Mosseri, J., Obernosterer, I., Park, Y.H., Picheral, M., Pondaven, P., Remenyi, T., Sandroni, V., Sarthou, G., Savoye, N., Scouarnec, L., Souhaut, M., Thuiller, D., Timmermans, K., Trull, T., Uitz, J., van Beek, P., Veldhuis, M., Vincent, D., Viollier, E., Vong, L., Wagener, T., 2007. Effect of natural iron fertilization on carbon sequestration in the Southern Ocean. Nature 446, 1070–1074.

Blain, S., Quéguiner, B., Trull, T., 2008. The natural iron fertilization experiment KEOPS (KErguelen Ocean and Plateau compared Study): An overview. Deep Sea Res. Part II 55, 559–565.

Boutorh, J., Moriceau, B., Gallinari, M., Ragueneau, O., Bucciarelli, E., 2016. Effect of trace metal-limited growth on the postmortem dissolution of the marine diatom *Pseudo-nitzschia delicatissima*. Global Biogeochem. Cycles 30, 57–69.

Bundy, R.M., Biller, D.V., Buck, K.N., Bruland, K.W., Barbeau, K.A., 2014. Distinct pools of dissolved iron-binding ligands in the surface and benthic boundary layer of the California Current. Limnol. Oceanogr. 59, 769–787.

Burdige, D.J., 1993. The biogeochemistry of manganese and iron reduction in marine sediments. Earth Sci. Rev. 35, 249–284.

Cheize, M., Planquette, H.F., Fitzsimmons, J.N., Pelleter, E., Sherrell, R.M., Lambert, C., Bucciarelli, E., Sarthou, G., Le Goff, M., Liorzou, C., Chéron, S., Viollier, E., Gayet, N., 2019. Contribution of resuspended sedimentary particles to dissolved iron and manganese in the ocean: An experimental study. Chem. Geol. 511, 389–415.

Chester, R., Jickells, T., 2012. The Transport of Material to the Oceans: Relative Flux Magnitudes. In: Chester, R., Jickells, T. (Eds.), Marine Geochemistry. John Wiley & Sons Ltd, pp. 92–124.

Colombo, M., Rogalla, B., Li, J., Allen, S.E., Orians, K.J., Maldonado, M.T., 2021. Canadian Arctic Archipelago Shelf-Ocean Interactions: A Major Iron Source to Pacific Derived Waters Transiting to the Atlantic. Global Biogeochem. Cycles 35.

Conway, T.M., John, S.G., 2014. Quantification of dissolved iron sources to the North Atlantic Ocean. Nature 511, 212–215.

Conway, T.M., Rosenberg, A.D., Adkins, J.F., John, S.G., 2013. A new method for precise determination of iron, zinc and cadmium stable isotope ratios in seawater by double-spike mass spectrometry. Anal. Chim. Acta 793, 44–52.

Conway, T.M., Palter, J.B., de Souza, G.F., 2018. Gulf Stream rings as a source of iron to the North Atlantic subtropical gyre. Nat. Geosci. 11, 594–598.

Craddock, P.R., Dauphas, N., 2011. Iron Isotopic Compositions of Geological Reference Materials and Chondrites. Geostand. Geoanal. Res. 35, 101–123.

Dale, A.W., Nickelsen, L., Scholz, F., Hensen, C., Oschlies, A., Wallmann, K., 2015. A revised global estimate of dissolved iron fluxes from marine sediments. Global Biogeochem. Cycles 29, 691–707.

de Baar, de Jong, 2001. Distributions, sources and sinks of iron in seawater. In: Turner, D., Hunter, K.A. (Eds.), Biogeochemistry of Iron in Seawater. Wiley, pp. 123–253.

de Jonge, M.D., Holzner, C., Baines, S.B., Twining, B.S., Ignatyev, K., Diaz, J., Howard, D.L., Legnini, D., Miceli, A., McNulty, I., Jacobsen, C.J., Vogt, S., 2010. Quantitative 3D elemental microtomography of Cyclotella meneghiniana at 400-nm resolution. Proc. Natl. Acad. Sci. U.S.A. 107, 15676–15680.

Dideriksen, K., Baker, J.A., Stipp, S.L.S., 2008. Equilibrium Fe isotope fractionation between inorganic aqueous Fe(III) and the siderophore complex, Fe(III)-desferrioxamine B. Earth Planet. Sci. Lett. 269, 280–290.

Dove, L.A., Thompson, A.F., Balwada, D., Gray, A.R., 2021. Observational Evidence of Ventilation Hotspots in the Southern Ocean. J. Geophys. Res. Oceans 126.

Ellwood, M.J., Hunter, K.A., 2000. The incorporation of zinc and iron into the frustule of the marine diatom Thalassiosira pseudonana. Limnol. Oceanogr. 45, 1517–1524.

Ellwood, M.J., Hutchins, D.A., Lohan, M.C., Milne, A., Nasemann, P., Nodder, S.D., Sander, S.G., Strzepek, R., Wilhelm, S.W., Boyd, P.W., 2015. Iron stable isotopes track pelagic iron cycling during a subtropical phytoplankton bloom. Proc. Natl. Acad. Sci. U.S.A. 112, E15–E20.

Ellwood, M.J., Strzepek, R.F., Strutton, P.G., Trull, T.W., Fourquez, M., Boyd, P.W., 2020. Distinct iron cycling in a Southern Ocean eddy. Nat. Commun. 11, 825.

Elrod, V.A., Berelson, W.M., Coale, K.H., Johnson, K.S., 2004. The flux of iron from continental shelf sediments: A missing source for global budgets. Geophys. Res. Lett. 31 n/a–n/a.

Félix-Bermúdez, A., Delgadillo-Hinojosa, F., Torres-Delgado, E.V., Muñoz-Barbosa, A., 2020. Does Sea Surface Temperature Affect Solubility of Iron in Mineral Dust? The Gulf of California as a Case Study. J. Geophys. Res. Oceans 125 e2019JC015999.

Fitzsimmons, J.N., John, S.G., Marsay, C.M., Hoffman, C.L., Nicholas, S.L., Toner, B.M., German, C.R., Sherrell, R.M., 2017. Iron persistence in a distal hydrothermal plume supported by dissolved–particulate exchange. Nat. Geosci. 10, 195–201.

Gardner, W.D., Richardson, M.J., Mishonov, A.V., 2018. Global assessment of benthic nepheloid layers and linkage with upper ocean dynamics. Earth Planet. Sci. Lett. 482, 126–134.

Gledhill, M., Buck, K.N., 2012. The organic complexation of iron in the marine environment: a review. Front. Microbiol. 3, 69.

Goldberg, E.D., 1954. Marine Geochemistry. 1. Chemical Scavengers of the Sea. J. Geol. 62, 249–265.

González-Santana, D., Planquette, H., Cheize, M., Whitby, H., Gourain, A., Holmes, T., Guyader, V., Cathalot, C., Pelleter, E., Fouquet, Y., Sarthou, G., 2020. Processes Driving Iron and Manganese Dispersal From the TAG Hydrothermal Plume (Mid-Atlantic Ridge): Results From a GEOTRACES Process Study. Front. Mar. Sci. 7.

Greenwood, J.E., Truesdale, V.W., Rendell, A.R., 2001. Biogenic silica dissolution in seawater — in vitro chemical kinetics. Prog. Oceanogr. 48, 1–23.

Gross, T.F., Williams, A.J., Newell, A.R.M., 1988. A deep-sea sediment transport storm. Nature 331, 518–521.

Hammond, D.E., Cummins, K.M., McManus, J., Berelson, W.M., Smith, G., Spagnoli, F., 2004. Methods for measuring benthic nutrient flux on the California Margin: Comparing shipboard core incubations to in situ lander results. Limnol. Oceanog. Methods 2, 146–159.

Hatta, M., Measures, C.I., Selph, K.E., Zhou, M., Hiscock, W.T., 2013. Iron fluxes from the shelf regions near the South Shetland Islands in the Drake Passage during the austral-winter 2006. Deep Sea Res. Part II 90, 89–101.

Henkel, S., Kasten, S., Poulton, S.W., Staubwasser, M., 2016. Determination of the stable iron isotopic composition of sequentially leached iron phases in marine sediments. Chem. Geol. 421, 93–102.

Henkel, S., Kasten, S., Hartmann, J.F., Silva-Busso, A., Staubwasser, M., 2018. Iron cycling and stable Fe isotope fractionation in Antarctic shelf sediments, King George Island. Geochim. Cosmochim. Acta 237, 320–338.

Homoky, W.B., Severmann, S., Mills, R.A., Statham, P.J., Fones, G.R., 2009. Pore-fluid Fe isotopes reflect the extent of benthic Fe redox recycling: Evidence from continental shelf and deep-sea sediments. Geology 37, 751–754.

Homoky, W.B., Severmann, S., McManus, J., Berelson, W.M., Riedel, T.E., Statham, P.J., Mills, R.A., 2012. Dissolved oxygen and suspended particles regulate the benthic flux of iron from continental margins. Mar. Chem. 134–135, 59–70.

Homoky, W.B., Conway, T.M., John, S.G., König, D., Deng, F., Tagliabue, A., Mills, R.A., 2021. Iron colloids dominate sedimentary supply to the ocean interior. Proc. Natl. Acad. Sci. U.S.A. 118, e2016078118.

Homoky, W.B., John, S.G., Conway, T.M., Mills, R.A., 2013. Distinct iron isotopic signatures and supply from marine sediment dissolution. Nat. Commun. 4.

Hopwood, M.J., Statham, P.J., Skrabal, S.A., Willey, J.D., 2015. Dissolved iron(II) ligands in river and estuarine water. Mar. Chem. 173, 173–182.

Horner, T., Little, S., Conway, T., Farmer, J., Hertzberg, J., Lough, A., McKay, J., Tessin, A., Galer, S., Jaccard, S., Lacan, F., Paytan, A., Wuttig, K., Bolton, C., Calvo, E., Cardinal, D., de Garidel-Thoron, T., Fietz, S., Hendry, K., Marcantonio, F., Rafter, P., Ren, H., Somes, C., Sutton, J., Torfstein, A., Winckler, G., 2020. Bioactive trace metals and their isotopes as paleoproductivity proxies: An assessment using GEOTRACES-era data. Global Biogeochem. Cycles 35, 12.

Ingall, E.D., Diaz, J.M., Longo, A.F., Oakes, M., Finney, L., Vogt, S., Lai, B., Yager, P.L., Twining, B.S., Brandes, J.A., 2013. Role of biogenic silica in the removal of iron from the Antarctic seas. Nat. Commun. 4, 1981.

Jeandel, C., 2016. Overview of the mechanisms that could explain the 'Boundary Exchange' at the land-ocean contact. Phil. Trans. R. Soc. A 374.

Jeandel, C., Peucker-Ehrenbrink, B., Jones, M.T., Pearce, C.R., Oelkers, E.H., Godderis, Y., Lacan, F., Aumont, O., Arsouze, T., 2011. Ocean margins: The missing term in oceanic element budgets? Eos Trans. AGU 92, 217–218.

Jensen, L.T., Morton, P., Twining, B.S., Heller, M.I., Hatta, M., Measures, C.I., John, S., Zhang, R., Pinedo-Gonzalez, P., Sherrell, R.M., Fitzsimmons, J.N., 2020. A comparison of marine Fe and Mn cycling: U.S. GEOTRACES GN01 Western Arctic case study. Geochim. Cosmochim. Acta 288, 138–160.

Jickells, T.D., An, Z.S., Andersen, K.K., Baker, A.R., Bergametti, G., Brooks, N., Cao, J.J., Boyd, P.W., Duce, R.A., Hunter, K.A., Kawahata, H., Kubilay, N., laRoche, J., Liss, P.S., Mahowald, N., Prospero, J.M., Ridgwell, A.J., Tegen, I., Torres, R., 2005. Global

Iron Connections Between Desert Dust, Ocean Biogeochemistry, and Climate. Science 308, 67–71.

John, S.G., 2012. Optimizing sample and spike concentrations for isotopic analysis by double-spike ICPMS. J. Anal. At. Spectrom. 27.

John, S.G., Mendez, J., Moffett, J., Adkins, J., 2012. The flux of iron and iron isotopes from San Pedro Basin sediments. Geochim. Cosmochim. Acta 93, 14–29.

Klar, J.K., James, R.H., Gibbs, D., Lough, A., Parkinson, I., Milton, J.A., Hawkes, J.A., Connelly, D.P., 2017. Isotopic signature of dissolved iron delivered to the Southern Ocean from hydrothermal vents in the East Scotia Sea. Geology 45, 351–354.

König, D., Conway, T.M., Ellwood, M.J., Homoky, W.B., Tagliabue, A., 2021. Constraints on the cycling of iron isotopes from a global ocean model. Global Biogeochem. Cycles 35 e2021GB006968.

Labatut, M., Lacan, F., Pradoux, C., Chmeleff, J., Radic, A., Murray, J.W., Poitrasson, F., Johansen, A.M., Thil, F., 2014. Iron sources and dissolved-particulate interactions in the seawater of the Western Equatorial Pacific, iron isotope perspectives. Global Biogeochem. Cycles 28, 1044–1065.

Laës, A., Blain, S., Laan, P., Achterberg, E.P., Sarthou, G., de Baar, H.J.W., 2003. Deep dissolved iron profiles in the eastern North Atlantic in relation to water masses. Geophys. Res. Lett. 30 n/a–n/a.

Lagerström, M.E., Field, M.P., Séguret, M., Fischer, L., Hann, S., Sherrell, R.M., 2013. Automated on-line flow-injection ICP-MS determination of trace metals (Mn, Fe Co, Ni, Cu and Zn) in open ocean seawater: Application to the GEOTRACES program. Mar. Chem. 155, 71–80.

Lam, P.J., Heller, M.I., Lerner, P.E., Moffett, J.W., Buck, K.N., 2020. Unexpected Source and Transport of Iron from the Deep Peru Margin. ACS Earth Space Chem. 4, 977–992.

Landing, W.M., Bruland, K.W., 1987. The contrasting biogeochemistry of iron and manganese in the Pacific Ocean. Geochim. Cosmochim. Acta 51, 29–43.

Lee, J.-M., Lam, P.J., Vivancos, S.M., Pavia, F.J., Anderson, R.F., Lu, Y., Cheng, H., Zhang, P., Edwards, R.L., Xiang, Y., Webb, S.M., 2021. Changing chemistry of particulate material in the near- and far-field hydrothermal plumes from 15°S East Pacific Rise and its influence on metal scavenging. Geochim. Cosmochim. Acta 300, 95–118.

Lewis, B.L., Landing, W.M., 1991. The biogeochemistry of manganese and iron in the Black Sea. Deep Sea Res. Part A 38, S773–S803.

Liao, W.H., Takano, S., Yang, S.C., Huang, K.F., Sohrin, Y., Ho, T.Y., 2020. Zn Isotope Composition in the Water Column of the Northwestern Pacific Ocean: The Importance of External Sources. Global Biogeochem. Cycles 34.

Liao, W.-H., Takano, S., Tian, H.-A., Chen, H.-Y., Sohrin, Y., Ho, T.-Y., 2021. Zn elemental and isotopic features in sinking particles of the South China Sea: implications for its sources and sinks. Geochim. Cosmochim. Acta 314, 68–84.

Mackey, D.J., O`Sullivan, J.E.O., Watson, R.J., 2002. Iron in the western Pacific: a riverine or hydrothermal source for iron in the Equatorial Undercurrent? Deep Sea Res. Part I 49, 877–893.

Mendez, J., Guieu, C., Adkins, J., 2010. Atmospheric input of manganese and iron to the ocean: Seawater dissolution experiments with Saharan and North American dusts. Mar. Chem. 120, 34–43.

Milne, A., Schlosser, C., Wake, B.D., Achterberg, E.P., Chance, R., Baker, A.R., Forryan, A., Lohan, M.C., 2017. Particulate phases are key in controlling dissolved iron concentrations in the (sub)tropical North Atlantic. Geophys. Res. Lett. 44, 2377–2387.

Morgan, J.L., Wasylenki, L.E., Nuester, J., Anbar, A.D., 2010. Fe isotope fractionation during equilibration of Fe-organic complexes. Environ. Sci. Technol. 44, 6095–6101.

Moriceau, B., Goutx, M., Guigue, C., Lee, C., Armstrong, R., Duflos, M., Tamburini, C., Charrière, B., Ragueneau, O., 2009. Si–C interactions during degradation of the diatom Skeletonema marinoi. Deep Sea Res. Part II 56, 1381–1395.

Nishioka, J., Obata, H., Ogawa, H., Ono, K., Yamashita, Y., Lee, K., Takeda, S., Yasuda, I., 2020. Subpolar marginal seas fuel the North Pacific through the intermediate water

at the termination of the global ocean circulation. Proc. Natl. Acad. Sci. U.S.A. 117, 12665–12673.

Poulton, S.W., Raiswell, R., 2002. The low-temperature geochemical cycle of iron: From continental fluxes to marine sediment deposition. Am. J. Sci. 302, 774–805.

Pratihary, A.K., Naqvi, S.W.A., Narvenkar, G., Kurian, S., Naik, H., Naik, R., Manjunatha, B.R., 2014. Benthic mineralization and nutrient exchange over the inner continental shelf of western India. Biogeosciences 11, 2771–2791.

Puig, P., Madron, X.D.D., Salat, J., Schroeder, K., Martín, J., Karageorgis, A.P., Palanques, A., Roullier, F., Lopez-Jurado, J.L., Emelianov, M., Moutin, T., Houpert, L., 2013. Thick bottom nepheloid layers in the western Mediterranean generated by deep dense shelf water cascading. Prog. Oceanogr. 111, 1–23.

Radic, A., Lacan, F., Murray, J.W., 2011. Iron isotopes in the seawater of the equatorial Pacific Ocean: New constraints for the oceanic iron cycle. Earth Planet. Sc. Lett. 306, 1–10.

Raven, J.A., Geider, R.J., 1988. Temperature and algal growth. New Phytol. 110, 441–461.

Roshan, S., DeVries, T., Wu, J., John, S., Weber, T., 2020. Reversible scavenging traps hydrothermal iron in the deep ocean. Earth Planet. Sc. Lett. 542.

Rouxel, O.J., Auro, M., 2010. Iron Isotope Variations in Coastal Seawater Determined by Multicollector ICP-MS. Geostand. Geoanal. Res. 34, 135–144.

Severmann, S., McManus, J., Berelson, W.M., Hammond, D.E., 2010. The continental shelf benthic iron flux and its isotope composition. Geochim. Cosmochim. Acta 74, 3984–4004.

Siebert, C., Nägler, T.F., Kramers, J.D., 2001. Determination of molybdenum isotope fractionation by double-spike multicollector inductively coupled plasma mass spectrometry. Geochem. Geophys. Geosyst. 2 n/a–n/a.

Sohrin, Y., Urushihara, S., Nakatsuka, S., Kono, T., Higo, E., Minami, T., Norisuye, K., Umetani, S., 2008. Multielemental determination of GEOTRACES key trace metals in seawater by ICPMS after preconcentration using an ethylenediaminetriacetic acid chelating resin. Anal. Chem. 80, 6267–6273.

Tagliabue, A., Aumont, O., DeAth, R., Dunne, J.P., Dutkiewicz, S., Galbraith, E., Misumi, K., Moore, J.K., Ridgwell, A., Sherman, E., Stock, C., Vichi, M., Völker, C., Yool, A., 2016. How well do global ocean biogeochemistry models simulate dissolved iron distributions? Global Biogeochem. Cycles 30, 149–174.

Tessin, A., März, C., Blais, M.A., Brumsack, H.J., Matthiessen, J., O'Regan, M., Schnetger, B., 2020. Arctic continental margin sediments as possible fe and mn sources to seawater as sea ice retreats: insights from the Eurasian Margin. Global Biogeochem. Cycles 34.

Tonnard, M., Planquette, H., Bowie, A.R., van der Merwe, P., Gallinari, M., Desprez de Gésincourt, F., Germain, Y., Gourain, A., Benetti, M., Reverdin, G., Tréguer, P., Boutorh, J., Cheize, M., Lacan, F., Menzel Barraqueta, J.-L., Pereira-Contreira, L., Shelley, R., Lherminier, P., Sarthou, G., 2020. Dissolved iron in the North Atlantic Ocean and Labrador Sea along the GEOVIDE section (GEOTRACES section GA01). Biogeosciences 17, 917–943.

Twining, B.S., Baines, S.B., 2013. The Trace Metal Composition of Marine Phytoplankton. Annu. Rev. Mar. Science 5, 191–215.

Van Cappellen, P., Viollier, E., Roychoudhury, A., Clark, L., Ingall, E., Lowe, K., Dichristina, T., 1998. Biogeochemical Cycles of Manganese and Iron at the Oxic−Anoxic Transition of a Stratified Marine Basin (Orca Basin, Gulf of Mexico). Environ. Sci. Technol. 32, 2931–2939.

van der Merwe, P., Bowie, A.R., Quéroué, F., Armand, L., Blain, S., Chever, F., Davies, D., Dehairs, F., Planchon, F., Sarthou, G., Townsend, A.T., Trull, T.W., 2015. Sourcing the iron in the naturally fertilised bloom around the Kerguelen Plateau: particulate trace metal dynamics. Biogeosciences 12, 739–755.

Weyer, S., Schwieters, J.B., 2003. High precision Fe isotope measurements with high mass resolution MC-ICPMS. Int. J. Mass Spectrom. 226, 355–368.